JOURNAL OF GEOPHYSICAL RESEARCH: ATMOSPHERES, VOL. 118, 1–15, doi:10.1002/jgrd.50687, 2013

Timescale dependence of aeolian sand flux observations under atmospheric turbulence

Raleigh L. Martin,[1] Thomas E. Barchyn,[2] Chris H. Hugenholtz,[2]
and Douglas J. Jerolmack[1]

Received 9 March 2013; revised 24 July 2013; accepted 26 July 2013.

[1] The transport of sand in saltation is driven by the persistently unsteady stresses exerted by turbulent winds. Based on coupled high-frequency observations of wind velocity and sand flux on a desert dune during intermittent saltation, we show here how observations of saltation by natural winds depend significantly on the timescale and method used for determining shear stress and sand flux. The correlation between sand flux and excess shear stress (stress above a threshold value) systematically improves for longer averaging timescale, T, and is better for stress determined by the law-of-the-wall versus the Reynolds stress method. Fitting parameters for the stress-flux relationship do not converge with increasing T, which may be explained by the nonstationary nature of wind velocity statistics. We show how it may be possible, based on the scale-dependent statistics of stress fluctuations, to rescale saltation flux predictions for wind observations made at different timescales. However, our observations indicate hysteresis and time lags in thresholds for initiation and cessation of saltation, which complicate threshold-based approaches to predicting sediment transport at different timescales.

Citation: Martin, R. L., T. E. Barchyn, C. H. Hugenholtz, and D. J. Jerolmack (2013), Timescale dependence of aeolian sand flux observations under atmospheric turbulence, *J. Geophys. Res. Atmos.*, *118*, doi:10.1002/jgrd.50687.

1. Introduction

[2] Determining how surface winds drive aeolian sediment transport is important for understanding the evolution of dune fields [e.g., *Bagnold*, 1941] and the generation of aerosols affecting climate [e.g., *Kok*, 2011]. Wind moves sand primarily through the hopping motion of saltation [e.g., *Bagnold*, 1941; *Kok et al.*, 2012], which is important both as the driver of landform evolution [e.g., *Duran et al.*, 2011] and as the stimulant of dust detachment [e.g., *Lu and Shao*, 1999]. Many researchers have offered equilibrium relationships to predict aeolian saltation flux [e.g., *Bagnold*, 1941; *Kawamura*, 1951; *Owen*, 1964; *Lettau and Lettau*, 1977; *Ungar and Haff*, 1987; *Sorensen*, 2004; *Pahtz et al.*, 2012]; however, these relationships often disagree substantially with field observations [e.g., *Sherman et al.*, 1998; *Sherman and Li*, 2012].

[3] Equilibrium saltation flux laws assume "saturation," such that momentum fluxes to and from the cloud of saltators are balanced [e.g., *Duran et al.*, 2011]. While it is easy to achieve steady state conditions in the wind tunnel, the ubiquity of large coherent turbulent structures and meteorological variability suggests that atmospheric surface layer (ASL) winds may never exhibit true steady state behavior [*Metzger et al.*, 2007]. Accounting for these turbulent effects cannot depend simply on improving the resolution of field observation; in fact, high-frequency wind and sediment observations often display particularly poor correlation [*Bauer et al.*, 1998; *Sterk et al.*, 1998; *Schonfeldt and von Lowis*, 2003]. It appears that such disagreement arises due to the lagged response of sediment flux to wind [e.g., *Anderson and Haff*, 1988; *McEwan and Willetts*, 1993; *Gillette et al.*, 1996] and the presence of separate "aerodynamic" and "collision" thresholds for initiation and cessation of motion, respectively [e.g., *Bagnold*, 1941; *Kok*, 2010]. Predicting aeolian sand flux therefore depends on understanding not only equilibrium but also transient response to turbulent wind [*Fan and Disrud*, 1977; *Sorensen*, 1997; *Namikas et al.*, 2003; *Schonfeldt and von Lowis*, 2003]. Coupled field observation of wind and saltation flux offers the potential to reach this understanding [*Butterfield*, 1991; *Jackson and McCloskey*, 1997; *Baas*, 2006; *Bauer et al.*, 1998; *Sterk et al.*, 1998; *Schonfeldt and von Lowis*, 2003; *Leenders et al.*, 2005], but proper interpretation of such records requires careful consideration of the interplay between atmospheric turbulence and saltation [e.g., *Baas and Sherman*, 2005; *Baas*, 2006].

[4] Aeolian saltation models generally consider the dependence of sand mass flux, Q, on wind shear stress, τ, or shear velocity, U_*, in excess of a threshold value. Field measurements to validate and parameterize saltation

---

[1] Department of Earth and Environmental Science, University of Pennsylvania, Philadelphia, Pennsylvania, USA.
[2] Department of Geography, University of Lethbridge, Lethbridge, Alberta, Canada.

Corresponding author: R. L. Martin, Department of Earth and Environmental Science, University of Pennsylvania, Philadelphia, PA 19104, USA. (raleighm@sas.upenn.edu)

2169-897X/13/10.1002/jgrd.50687

models thus depend on measuring these quantities. In addition to basic technical challenges in measuring sand fluxes and wind velocities [e.g., *Ellis et al.*, 2009], field determination of shear stress is complicated by turbulent fluctuations in wind velocity [e.g., *van Boxel et al.*, 2004; *Walker*, 2005], the tendency of saltating particles to extract momentum from the near-surface wind [e.g., *McKenna Neuman and Nickling*, 1994; *Li and McKenna Neuman*, 2012], and modifications to wind profiles over complex topography [e.g., *Jackson and Hunt*, 1975; *Hogstrom et al.*, 2002; *Chapman et al.*, 2012]. As a result, interpretation of the Q-τ relationship depends on how we define and measure shear stress. Different methods of estimating τ incorporate different assumptions about spatial and temporal averaging [*Namikas et al.*, 2003; *Guo et al.*, 2012]. Before we can systematically address equilibrium and transient sand flux predictions in nature, we must first consider the scale-dependent effects of such averaging in relation to the physics of saltation.

[5] In this article, we consider, on the basis of coupled high-frequency observations of saltation flux and wind velocity, how derivation of the Q-τ relationship depends on choice of time-averaging interval and method for computation of shear stress. We relate these averaging effects to timescale dependence of stress computations during turbulent winds and intermittent saltation. Finally, tentative ideas are offered for addressing scale dependence in prediction of aeolian sand flux in natural environments.

2. Theory

2.1. Shear Stress Estimation

[6] Two methods, (1) the logarithmic law-of-the-wall ("log law") and (2) turbulent Reynolds stress, are usually employed to compute wind shear stress. According to the log law [*von Karman*, 1930], mean horizontal wind velocity, $U(z)$, as a function of height, z, is given by

$$U(z) = \frac{U_*}{\kappa} \ln \frac{z}{z_0}. \quad (1)$$

κ is the von Karman constant ($\kappa = 0.4$), and z_0 is the aerodynamic roughness height. Shear velocity, U_*, is related to τ as follows:

$$\tau_{\log} = \rho_a U_*^2, \quad (2)$$

where ρ_a is air density (1.23 kg/m^3), and $\tau_{\log}$ denotes computation of τ based on U_* from the log law. Assuming neutrally stable conditions, the log law is usually valid within the lowest 10–15% of a canonical boundary layer [*Li and McKenna Neuman*, 2012] or neutral ASL [*Metzger et al.*, 2007], though complex topography may locally modify wind profiles [e.g., *Arens et al.*, 1995]. Modifications to the log law under non-neutral stability are described by the Monin-Obukhov similarity laws [e.g., *Kaimal and Finnigan*, 1994].

[7] The log law provides an estimate of the height-averaged near-surface shear stress, based on a fit to the time-averaged vertical profile of the wind velocity. In contrast, the Reynolds stress estimates τ at a single height, based on covarying fluctuations of horizontal and vertical wind describing the downward passage of fluid momentum by turbulent eddies [e.g., *van Boxel et al.*, 2004]:

$$\tau_{Re} = \langle -\rho_a u' w' \rangle. \quad (3)$$

Here τ_{Re} refers to shear stress computed by the Reynolds stress method, and u' and w' refer to the instantaneous fluctuating components of streamwise and vertical wind, respectively, i.e.,

$$u'(t) = u(t) - U, \quad (4)$$

$$w'(t) = w(t) - W. \quad (5)$$

u and U (w and W) are the instantaneous and time-averaged streamwise (vertical) winds, respectively. The angle brackets, $\langle\rangle$, in equation (3) (and subsequently in this article) denote a mean over many observations.

2.2. Aerodynamic Roughness Height

[8] Determination of shear stress by the log law in equation (1) requires either wind speed measurements at multiple heights or measurements of wind speed at a single height with assumption of a roughness height, z_0. However, z_0 grows systematically with U_* as saltation extracts momentum and modifies the wind velocity profile [*Owen*, 1964; *Sherman*, 1992; *Sherman and Farrell*, 2008; *Pahtz et al.*, 2012]. One way to circumvent this complication is by adopting a modified version of the log law as done by *Bagnold* [1941]. It has been noted that, during saltation transport, the streamwise wind velocity at a "focal height," z_f, converges to a constant time-averaged focal velocity, U_f, irrespective of the free-stream wind velocity [e.g., *Owen*, 1964]. In particular, *Bagnold* [1941] found that $z_f \approx 3$ mm during active saltation in a wind tunnel, while $z_f \approx 1$ cm under natural saltation [*Bagnold*, 1938]. Other investigators have observed focal heights ranging from ≈ 2 mm to ≈ 2 cm [*Werner*, 1990; *Rasmussen and Sorensen*, 2008; *Duran et al.*, 2011], and it appears likely that suppression of large eddies by wind tunnels may reduce the focal height compared to natural saltation [*Sherman and Farrell*, 2008]. Above the near-bed region ($\approx 0 - 2$ cm) where intense saltation extracts significant momentum from the wind [e.g., *Bauer et al.*, 2004], the wind velocity profile should retain the same logarithmic slope and U_* as if under "clean air" conditions, except that now the entire profile is shifted upward based on the focal height [*Bagnold*, 1941]. Given this apparent constancy of z_f and U_f, we can adopt a modified log law [*Bagnold*, 1941; *Owen*, 1964]:

$$U(z) - U_f = \frac{U_*}{\kappa} \ln \frac{z}{z_f}. \quad (6)$$

This equation applies when saltation is active, while equation (1) is valid during intervals of no transport. Taken together, equations (1) and (6) give a piecewise dependence of U_* on the measured horizontal wind, which we calculate as follows:

$$U_* = \begin{cases} \frac{\kappa U}{\ln(z/z_0)} & \text{if } U_* < U_{*,c}, \\ \frac{\kappa (U - U_f)}{\ln(z/z_f)} & \text{if } U_* \geq U_{*,c}. \end{cases} \quad (7)$$

The equation above requires estimation of z_0, z_f, and U_f, and it assumes a single threshold shear velocity, $U_{*,c}$, corresponding to the onset of saltation.

2.3. Time Averaging

[9] Calculation of τ by the log law and Reynolds stress methods requires time averaging in computation of U and W, as these methods must incorporate the full range of turbulent eddies to be strictly valid. Defining T as the averaging time, we compute window-averaged time series of streamwise wind velocity, U^T, as follows:

$$U^T(t) = \int_{t-T/2}^{t+T/2} u(s)\mathrm{d}s, \tag{8}$$

where s is a dummy variable for the integration. An identical calculation can be performed for window-averaged vertical velocity, W^T. We define U_*^T and $\tau_{\log}^T$ as the corresponding shear velocity and shear stress computed by equations (7) and (2), respectively, based on U^T. Similarly, we define τ_{Re}^T as the Reynolds stress calculated by equation (3) using U^T and W^T in equations (4) and (5), respectively. We note that in most wind tunnel studies, where stationarity in the wind velocity time series can safely be assumed, T is simply taken as the duration of the measured time series [e.g., *Li and McKenna Neuman*, 2012].

2.4. Saltation Flux Scaling

[10] There is currently much controversy regarding the appropriate model to relate shear stress and aeolian sediment flux [e.g., *Kok et al.*, 2012]. Flux laws typically consider how Q depends on τ in excess of a critical stress, τ_c, or critical shear velocity, $U_{*,c} = \sqrt{\tau_c/\rho_a}$, during equilibrium saltation in a homogeneous flow:

$$Q \propto (\tau - \tau_c)^n = (\tau_{\mathrm{ex}})^n, \tag{9}$$

where n is a scaling parameter, and $Q = 0$ for $\tau < \tau_c$. We define τ_{ex} as the "excess" shear stress. Equation (9) is a simplification, as many cited flux laws exhibit a more complex dependence on τ or U_* (See Table 1 in *Kok et al.* [2012] for a listing of such laws.). Nonetheless, much of the debate in aeolian saltation prediction revolves around the value of n in equation (9) [e.g., *Duran et al.*, 2011]. Most flux laws, beginning with *Bagnold* [1941], take $n = 3/2$ [e.g., *Kawamura*, 1951; *Lettau and Lettau*, 1977; *Namikas and Sherman*, 1997], though recent work suggests linear scaling with $n = 1$ [e.g., *Ungar and Haff*, 1987; *Ho et al.*, 2011]. Our intention here is not to test these flux laws; rather, we wish to show how time-averaging considerations can lead to problems in evaluation and parameterization of such relationships.

3. Field Observations and Methods

[11] We deployed instruments at White Sands National Monument, NM, USA, to measure high-frequency time series of wind and saltation on a sand dune. White Sands National Monument contains the world's largest gypsum dune field, which was formed by the deflation of the Pleistocene Lake Otero salt playa [*Langford*, 2003]. Instruments were situated on the upper stoss (slope $\approx$ 0.06) of an $\approx$ 8 m tall barchan dune in the central portion of the dune field (Universal Transverse Mercator (UTM) 13N 380590 3632185 as measured by Trimble differential GPS—see Figure 2 in *Jerolmack et al.* [2011] for relative map location). Grain size analysis by a Retsch Camsizer of gypsum sand collected from the ground at the site measured a slightly left-skewed lognormal distribution of particle diameter, with median, $D_{50} = 0.416$ mm, and 10th and 90th percentile diameters of $D_{10} = 0.229$ mm and $D_{90} = 0.575$ mm, respectively, similar to the grain size pattern observed by *Jerolmack et al.* [2011]. While interdunes at White Sands are wet and concreted together, sand on the dunes within a $\approx$ 50 m radius around the observation equipment was uniformly dry and noncohesive. High-frequency observations were made over the period of 14–18 h MST on 6 March 2012, during moderate southwesterly winds stimulating sand transport along the dominant dune field orientation.

[12] The field setup and configuration are shown in Figure 1. Wind velocity was measured by an RM Young 81000 Ultrasonic Anemometer, situated at 49 cm above the sediment bed, which recorded the three-dimensional wind vector within a 10 cm height by 10 cm diameter sampling volume at time interval of 0.1 s. The anemometer height was chosen as the lowest possible to avoid interference of saltating grains. Streamline correction was applied to the wind records as suggested by *van Boxel et al.* [2004], and for analysis we considered only the streamwise component, u, and neglected the transverse component, v, of horizontal wind, as wind direction changed little during the deployment. A vertical profile of saltation number flux was measured by a stack of seven Wenglor laser particle counters [*Hugenholtz and Barchyn*, 2011] located $\approx$ 0.7 m in the spanwise direction from the anemometer. Anemometer and Wenglor data were logged by a Campbell Scientific CR1000. While a shorter distance between Wenglor and anemometer observations would have been preferred for simultaneous comparisons, we chose the 0.7 m separation to minimize airflow interference between the instruments. Each Wenglor particle counter, which was set at its highest sensitivity ($\approx$ 40 μm) in accordance with past studies [e.g., *Hugenholtz and Barchyn*, 2011; *Davidson-Arnott et al.*, 2012; *Chapman et al.*, 2013], recorded the streamwise passage of discrete particles tripping a laser beam with $l_W = 30$ mm spanwise length and $h_W = 0.6$ mm height during a time interval of $T_W = 0.1$ s. We denote particle number counts recorded by the Wenglors as n_z, with z referring to the height of the instrument in mm above the bed surface. $z = 175, 132, 96, 66, 42, 25,$ and 10 mm for the seven measurement heights. The Wenglors were collectively attached to a wind vane allowing the instruments to rotate with general directional changes in the wind. In addition to the Wenglors, a "BSNE" sand trap [*Fryrear*, 1986], also attached to a wind vane and situated a further $\approx$ 0.45 m spanwise from the Wenglors, collected two time-integrated samples of saltation mass flux through a 20 mm spanwise by 50 mm vertical opening centered 100 mm above the bed surface. Sample time series of ultrasonic (streamline corrected) wind velocity components and Wenglor number counts are shown in Figure 1d. Grain sizes collected by the BSNE trap during Run 1 measured $D_{10} = 0.210$ mm, $D_{50} = 0.352$ mm, and $D_{90} = 0.489$ mm, somewhat smaller than that of the surface sample, reflecting a possible reduction in sediment size with saltation height [e.g., *Williams*, 1964]. Precision of all instrument heights at time of deployment was ±5 mm; additional changes in instrument height occurred with passage of $\approx$ 10 mm ripples. Four continuous records of wind velocity and saltation flux were generated over periods spanning

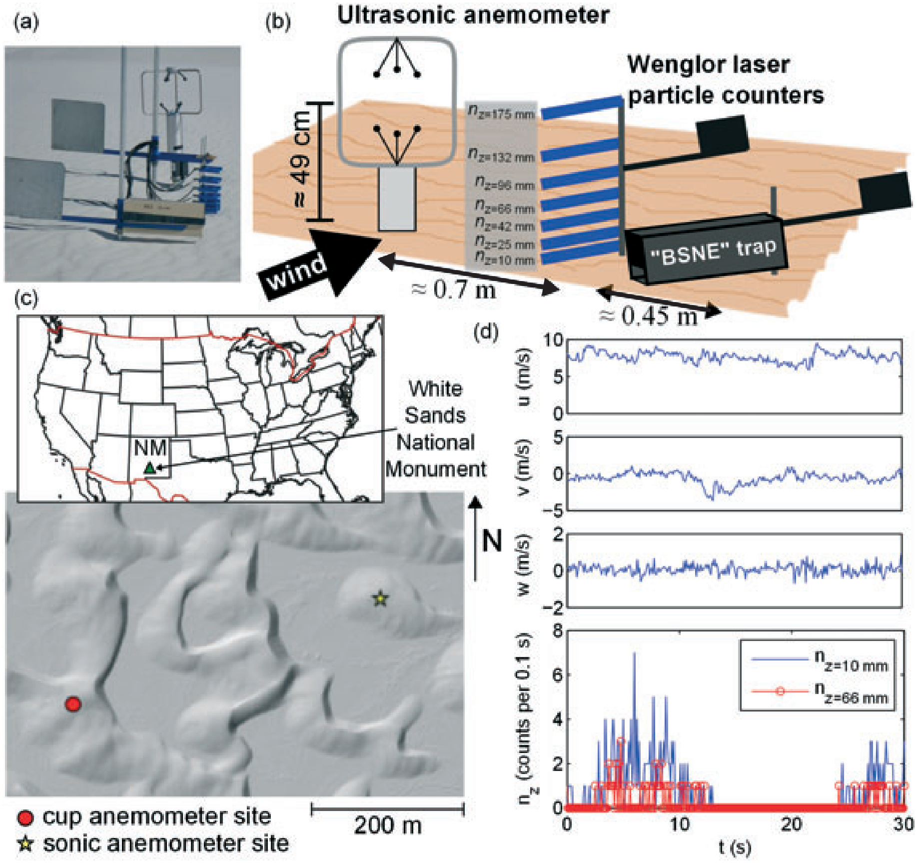

Figure 1. (a) Photo and (b) schematic diagram of field setup at White Sands National Monument, NM, USA, to measure high-frequency (10 Hz) wind velocity and saltation flux profile. (c) Location of White Sands National Monument and hillshade map of field site indicating locations of cup anemometer and high-frequency setup. (d) Time series of wind velocity (u,v,w—streamwise, transverse, and vertical wind, respectively) and particle number flux at two heights, $n_{z=10\text{mm}}$ and $n_{z=66\text{mm}}$, at the high-frequency measurement site. (Hillshade map in Figure 1c was generated from lidar data collected in 2010 by the National Center for Airborne Laser Mapping - http://dx.doi.org/10.5069/G97D2S2D.)

3084, 1568, 465, and 3277 s, respectively. At the beginning of each run, small sand accumulations were cleared from the instrument surfaces. The sand trap was emptied after Runs 1 and 4, giving two time-integrated sand flux estimates over durations of 3084 and 5610 s, respectively.

[13] We also considered observations of the wind profile by two RM Young 3001 cup anemometers deployed at a location (UTM 13N 380189 3632046) about 400 m west of the high-frequency observation site (Figure 1c). The cup anemometers were both attached to a vertical pole at heights of z_1 = 28.5 cm and z_2 = 185 cm above the ground surface, and the instruments again were positioned on the upper stoss slope of an ≈ 8 m dune. The cup anemometers recorded average wind velocities at 1 min increments over a period spanning 6 March 2012 18 h to 8 March 2012 10 h. The instruments did not measure wind direction but only the absolute magnitude of horizontal wind velocity. Surface grain size distributions at this site were similar to those at the high-frequency measurement site.

3.1. Determination of Saltation Flux

[14] We converted saltation number counts, n_z, to mass fluxes, q_z, by assuming spherical particles with diameter D = 0.352 mm (D_{50} of BSNE trap-collected sand at the site), sediment density of ρ_s = 2380 kg/m^3 for gypsum, flux cross-sectional area related to D and the Wenglor sensor height and length, h_W and l_W, respectively, and measurement time interval, T_W. Thus,

$$q_z = \left(\frac{\frac{1}{6}\pi D^3 \rho_s}{(h_W + D) l_W T_W} \right) n_z. \tag{10}$$

q_z, which has units of kg m^{-2}s^{-1}, describes a height-specific value of sediment flux. Figure 2a shows a profile of q_z values averaged over the duration of the field deployment.

[15] In agreement with past observation [*Williams*, 1964; *White*, 1982; *Greeley et al.*, 1996; *Namikas*, 2003; *Dong et al.*, 2012; *Farrell et al.*, 2012] and modeling [e.g., *Anderson and Hallet*, 1986], Figure 2a shows that the measured profile of q_z was roughly exponential, with a slight dip in flux near the surface, probably associated with interference of passing ripples with Wenglor sensors. Observations [e.g., *Namikas*, 2003] and models [e.g., *Duran et al.*, 2011] contrastingly find that near-surface sand flux exceeds exponential predictions, perhaps due to creep and reptation. We also noticed that $q_{z=96\text{mm}}$ systematically underestimated sediment flux compared to the expected profile, likely reflecting

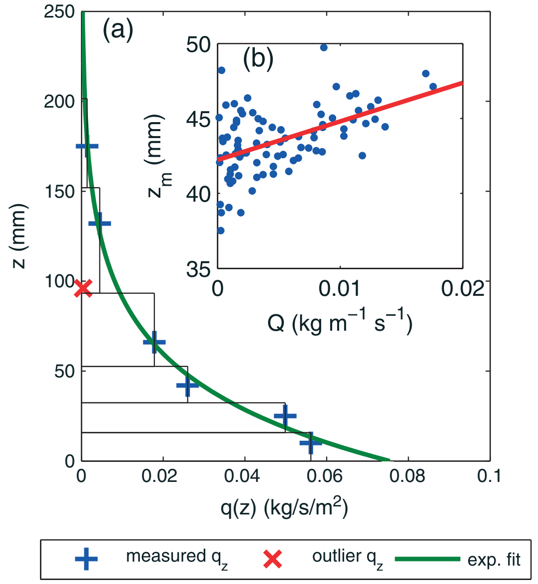

Figure 2. (a) Profile of saltation, $q(z)$, determined from the time average of all Wenglor measurements over the duration of the deployment. By convention, height above the bed, z, is shown on the ordinate axis even though it is the independent variable. Blue plus symbols show Wenglor observations corresponding to the q_z values computed by equation (10), while the red crosses indicate the outlier observation that we chose to ignore. The bars indicate summation for the calculation of height-integrated flux, Q, with the bar widths corresponding to the δz_i in equation (11). The solid green curve is an exponential fit; mean saltation height, z_m, predicted by this fit is 45 mm. (b) Mean saltation heights, z_m, estimated from 1 min averaged profiles of $q(z)$ versus total Q over the same interval. The data indicate some increase in z_m with Q; best-fit linear regression (red line) shows weak positive correlation ($R^2 = 0.25$).

instrumental error; thus, we chose to ignore this instrument in our analysis. Based on the six remaining Wenglors, we computed height-integrated saltation mass flux, Q, by taking a weighted sum of the individual fluxes, q_z, i.e.,

$$Q = \sum_i q_z \delta z_i. \tag{11}$$

As shown in Figure 2a, the δz_i were chosen so that boundaries between summation bins were equally spaced (in logarithmic space) between adjacent q_z heights. The upper limit for $q_{z=175\mathrm{mm}}$ was chosen to center this instrument within its logarithmic bin, while the bottom limit of $q_{z=10\mathrm{mm}}$ was taken as $z = 0$. Because the Wenglors were not equally spaced in logarithmic space, certain instruments were therefore more heavily weighted in the Q computation.

[16] To estimate the validity of our Wenglor flux predictions, we compared Wenglor-predicted total mass transport to BSNE trap measurements. Extrapolating from an exponential flux profile with constant $z_m = 45$ mm obtained from the exponential fit in Figure 2a, we estimated the total expected mass transport in the vertical range of the BSNE traps. Based on these calculations, the Wenglors predicted BSNE trap collections of 85.7 and 69.2 g for Run 1 and combined Runs 2–4, respectively. (Predictions for Runs 2–4 were interpolated to account for breaks in the Wenglor time series.) Actual BSNE measured values were 40.8 and 48.2 g, respectively, significantly smaller than observed. Such discrepancies may indicate issues with our calibration methods for estimating Wenglor flux [see *Hugenholtz and Barchyn*, 2011], but may also reflect trap inefficiency [e.g., *Greeley et al.*, 1996; *Rasmussen and Mikkelsen*, 1998] or problems in relating flux over the limited BSNE vertical range to total sediment flux. In calculating flux from the BSNE, we assumed constant z_m, while Figure 2b indicates that z_m increases slightly with Q. Linear regression to this relationship, shown in the figure, yields a weak positive correlation ($R^2 = 0.25$). There is ongoing debate about the physics determining z_m and whether z_m increases with Q [e.g., *Kok and Renno*, 2008]. *Almeida et al.* [2006] and *Dong et al.* [2012] observed increasing z_m with Q, while others [*Greeley et al.*, 1996; *Namikas*, 2003; *Creyssels et al.*, 2009] found a constant z_m. In addition to nonconstant z_m, variations in grain size with height might have also affected BSNE calibration, though such effects are subject to debate [e.g., *Williams*, 1964; *Farrell et al.*, 2012]. Irrespective of calibration issues, we believe that our high-frequency measurements provide accurate estimates of relative magnitudes of saltation flux through time [as in *Bauer et al.*, 2012].

4. Results

4.1. Determination of Parameters for the Log Law

[17] We begin by determining the parameters—aerodynamic roughness height, z_0, focal height, z_f, focal velocity, U_f, and critical shear velocity, $U_{*,c}$—required for estimation of shear velocity, U_*, by the piecewise log law in equation (7). To determine these parameters, we consider the cup anemometer wind profile observations. U_* can be computed directly from the logarithmic slope between the two instruments, i.e., $U_* = \frac{\kappa(U_2-U_1)}{\ln(z_2/z_1)}$, where U_1 and U_2 are the wind velocities at the z_1 and z_2 heights, respectively. We expect that for appropriate choice of z_f, equation (6) will give a constant value of U_f determined as follows:

$$U_f = \frac{U_1 - ZU_2}{1 - Z}, \tag{12}$$

where $Z = \frac{\ln(z_1/z_f)}{\ln(z_2/z_f)}$ is a constant. We performed the calculation in equation (12) for a range of z_f; the value minimizing changes in U_f with U_* was $z_f = 1.4$ mm, somewhat smaller than past observed focal heights. U_f computed with $z_f = 1.4$ mm is compared to observed U_* in Figure 3a. As can be seen, for U_* greater than a critical value of $U_{*,c} \approx 0.22$ m/s, focal velocity achieves a roughly constant mean value of $U_f = 3.8$ m/s, though the data show significant scatter around this value. When $U_* < 0.22$ m/s, however, U_f is not constant. We therefore interpret $U_{*,c} = 0.22$ m/s as the threshold for sediment transport in our system, which determines whether shear velocity is computed by the standard log law (equation (1)) or the modified log law (equation (6)). Based on equation (2), the critical shear stress corresponding to this value is $\tau_c = 0.060$ Pa.

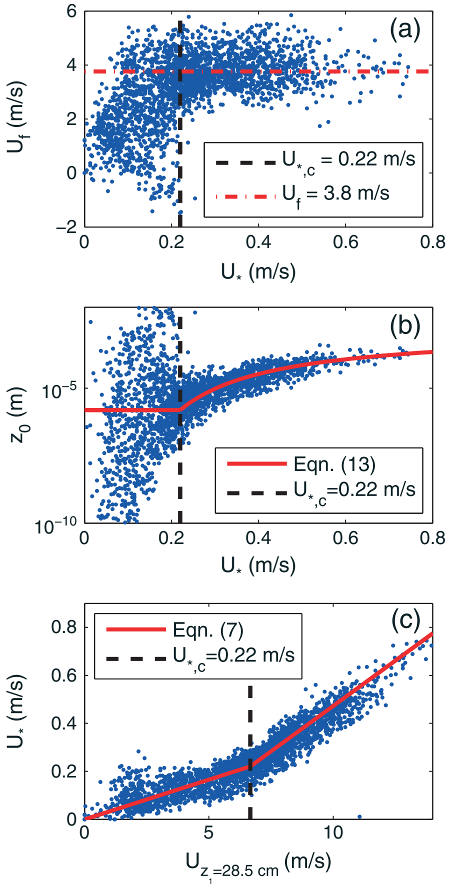

Figure 3. (a) Focal velocity, U_f, calculated by equation (12) for z_f = 1.4 mm, versus U_*, determined from the two anemometer vertical profile. When U_* exceeds an estimated critical shear velocity of $U_{*,c}$ = 0.22 m/s, the calculation yields a roughly constant focal velocity with mean U_f = 3.8 m/s, corresponding to periods of active saltation. (b) Observed values of z_0 computed by the log law (equation (1)) fit to two anemometer velocity profile compared to expected z_0 computed by equation (13). For $U_* < U_{*,c}$, a constant value of $z_0 = 1.5 \times 10^{-6}$ m is used. (c) Observed U_* from velocity profile versus simultaneous wind velocity measurements at lower cup anemometer, $U_{z_1=28.5}$ cm. Red line gives predictions from equation (7). Note the kink in the profile at $U_* = U_{*,c}$.

[18] By combining equations (1) and (6), we can estimate how the observed z_0 should increase with U_* when $U_* \geq U_{*,c}$:

$$z_0 = z_f \exp\left(-\frac{U_f \kappa}{U_*}\right). \tag{13}$$

Taking $U_* = U_{*,c}$ in the above equation yields an estimate of the "clean air" z_0, i.e., the constant roughness height when saltation is inactive and $U_* \leq U_{*,c}$. Taking $U_{*,c}$ = 0.22 m/s, we calculate $z_0 = 1.5 \times 10^{-6}$ m as the clean air roughness height. For comparison to these predicted values of z_0, we have plotted observed values of z_0 (computed from equation (1)) in Figure 3b. For $U_* < U_{*,c}$, observed z_0 ranges over many orders of magnitude, but the calculated $z_0 = 1.5 \times 10^{-6}$ m falls roughly in the middle of these observed values. For $U_* > U_{*,c}$, calculated z_0 increases systematically with U_* as expected by equation (13) and past observations [e.g., *McEwan and Willetts*, 1993]. We note here that a value of $z_0 = 10^{-4}$ m was observed by *Jerolmack et al.* [2006] at White Sands during active saltation when U_* = 0.41 m/s. For this U_*, our equation (13) predicts $z_0 = 3.4 \times 10^{-5}$ m, reasonably close to their measurement.

[19] Taking $z_0 = 1.5 \times 10^{-6}$ m, z_f = 1.4 mm, U_f = 3.8 m/s, and $U_{*,c}$ = 0.22 m/s as determined above, we utilize equation (7) to predict U_* based on wind velocities observed by the lower cup anemometer ($U_{z_1=28.5}$ cm). These predictions are compared to observed U_* values (determined from profile fit) in Figure 3c. The observations generally reproduce the predicted values of U_*, including the kink at $U_{*,c}$ expected by the piecewise nature of equation (7).

[20] Our analysis of the cup anemometer observations provides confidence that equation (7), which combines standard and modified versions of the log law, can be used to predict the shear velocity, U_*, based on observations of wind velocity at a single height above the bed. The values of z_0 and z_f used to parameterize equation (7) are somewhat smaller than expected from previous investigations, but the logarithmic dependence of U_* on z_0 and z_f means that the calculation is relatively insensitive to these values. Based on this observed validity of equation (7) for predicting U_* from cup anemometer wind velocity measured at a single height, we henceforth use equation (7) with the observed values of z_0, z_f, U_f, and $U_{*,c}$ to compute $\tau_{\log}$ from the sonic anemometer wind velocity observations made at a single height of z = 49 cm.

[21] We note that our computed "clean air" z_0 is significantly smaller than the Nikuradse $z_0 = D/30 \approx 10^{-5}$ m expectation [*Bagnold*, 1941]. It is possible that systematic changes in the apparent von Karman parameter [e.g., *Li et al.*, 2010], not accounted for in our measurements (which assume constant κ = 0.4), caused saltation intensity-dependent underestimation of U_* [*Sherman and Li*, 2012] and therefore underestimation of z_0 and z_f. We also note that usage of the log law (or modified log law) presumes that surface wind turbulence is dominantly generated by mechanical shear rather than by buoyancy. Unstable conditions may cause significant modification of the wind profile [e.g., *Frank and Kocurek*, 1994], requiring usage of similarity laws departing from the simple log law [e.g., *Kaimal and Finnigan*, 1994]. *Klose and Shao* [2012] and *Klose and Shao* [2013], for example, showed how inclusion of the convective contribution to surface shear stress can significantly modify modeled desert dust emissions. However, our data are insufficient to evaluate these von Karman and instability effects.

4.2. Q-τ Relationship

[22] We now consider the relationship between shear stress and sediment flux for varying durations of the time-averaging window. In our analysis, Q^T refers to window-averaged saltation flux computed over the same averaging time, T, used to compute corresponding average stress values, $\tau_{\log}^T$ and τ_{Re}^T. In analyzing the flux-stress relationship, we considered all four observational runs together. To eliminate moving-average bias, averaged values were computed over discrete (rather than moving) time windows; thus, larger values of T resulted in a reduced number of data points.

[23] Figure 4 compares $\tau_{\log}^T$, τ_{Re}^T and Q^T for four different values of T. The plots indicate progressive reduction in

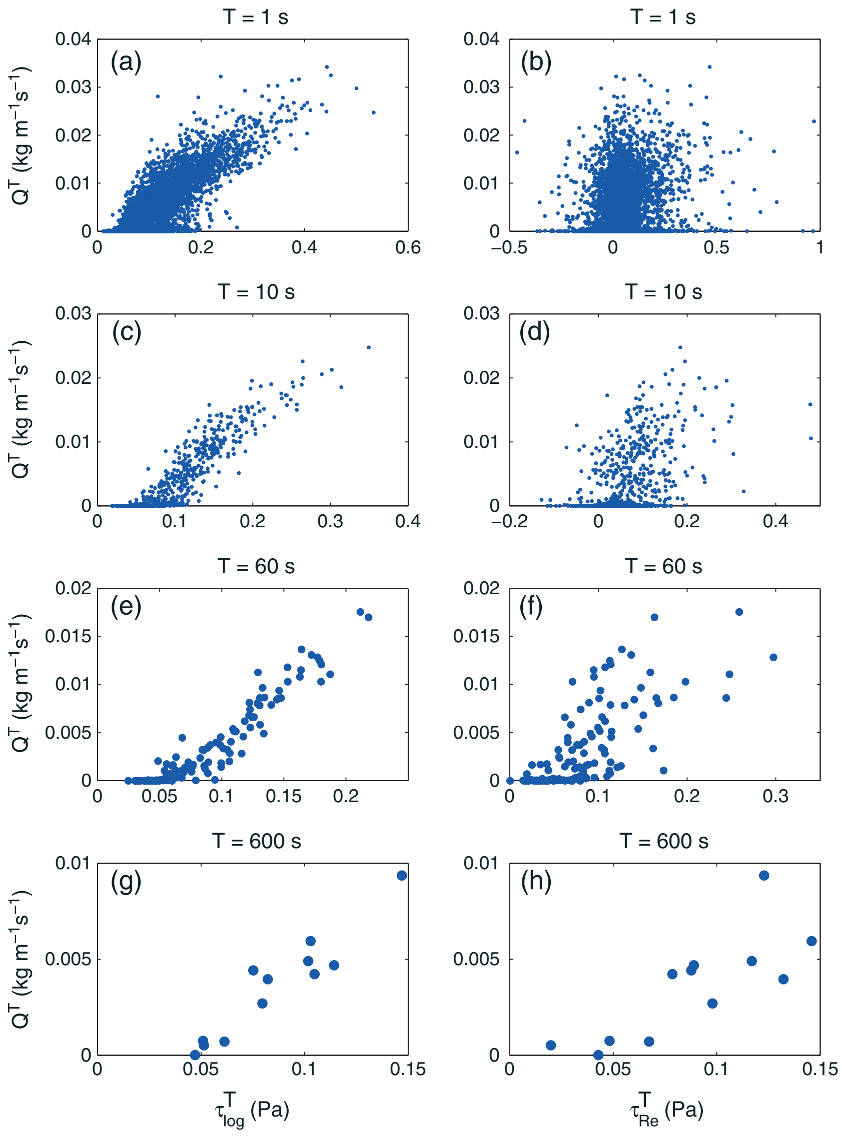

Figure 4. Q versus τ computed for four different averaging timescales, T. (a,c,e,g) Plots for the log law computed stress, $\tau_{\log}$; (b,d,f,h) plots for the Reynolds stress, τ_{Re}.

scatter of the Q versus τ relationship for increasing T. Figure 4a shows a distinctive rightward kink in the observation points, probably due to the piecewise nature of equation (7) for the modified log law. Figures 4b and 4d indicate a large number of negative τ_{Re} values, probably due to the short averaging time for computing Reynolds stress. Together, the plots in Figure 4 suggest a possible linear dependence of Q on $\tau_{\log}$ above a minimum threshold stress, while the form of the relationship for Q versus τ_{Re} is more indeterminate. Based on the possible linear scaling, for each T we applied least-squares regression to fit a line of the form:

$$Q^T_{\text{fit}} = C^T(\tau^T_{\log} - \tau^T_c), \tag{14}$$

where C^T and τ^T_c are fitting parameters associated with the timescale, T. We note here that calculated values of τ^T_c were allowed to differ from the value (τ_c = 0.060 Pa for $U_{*,c}$ = 0.22 m/s) assumed in equation (7) to compute U_*. To capture the linear transport regime, fitting was performed only for observations with $Q^T > 0$. An example of this linear fit is shown in Figure 5 for flux and log law stress values calculated with T = 60 s (as in Figure 4e). For this T, least-squares regression to equation (14) yielded parameters of $C^{T\text{=}60\text{s}}$ = 0.098 s and $\tau_c^{T\text{=}60s}$ = 0.055 Pa. For comparison, we also computed a fit of the form $Q = C_{3/2}(\tau_{\log} - \tau_c)^{3/2}$, which is shown in Figure 5 next to the linear fit. The 3/2 fit, which assumed $\tau_c^{T\text{=}60\text{s}}$ = 0.055 Pa from the linear fit, yielded a best-fit value of $C_{3/2}^{T\text{=}60\text{s}}$ = 0.39 m$^{1/2}$s^{2}kg$^{-1/2}$. As can be seen in the figure, both the linear and 3/2 relationship reasonably fit the data. In fact, when the linear and 3/2 predictions of Q are compared to observations, both relationships give a correlation coefficient of R^2 = 0.91.

[24] While both linear and 3/2 fits potentially explain the relationship between Q and τ, we choose to base further analysis on the linear relationship as the most parsimonious option for explaining the dependence of sediment flux on shear stress. In particular, we wish to consider how the fitting parameters C^T and τ^T_c in equation (14) vary with the choice

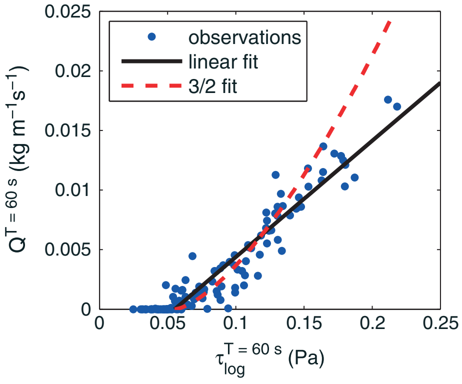

Figure 5. $Q^{T=60s}$ versus $\tau_{\log}^{T=60s}$, as in Figure 4e. Solid black line shows a linear regression of the form $Q = C(\tau_{\log} - \tau_c)$. Dashed red line shows a fit to $Q = C_{3/2}(\tau_{\log} - \tau_c)^{3/2}$. Methods for fitting curves are described in section 4.2. $R^2 = 0.91$ for both linear and 3/2 fits.

of averaging timescale, T, for linear regression to the Q^T versus $\tau_{\log}^T$ relationship. (We henceforth ignore comparisons of Q^T to τ_{Re}^T, based on their relatively poor performance.) Figure 6 shows how τ_c^T and C^T, fit to equation (14), vary with T. τ_c^T increases dramatically with T up to $\approx$ 10 s, then gradually declines. Values of C^T increase with T up to about 60 s, then decline gradually, though the relative changes in C^T with T are small compared to that for τ_c^T. Most importantly, there is no convergence in the stress-flux relationship apparent at any timescale.

[25] Previous researchers [e.g., *Shao and Mikami*, 2005] have noted the reduced scatter in the aeolian flux relationship with increasing timescale. Here we seek to quantify and explain this effect. We assess the timescale dependence of scatter in the Q-τ relationship by considering the mean-squared difference of observed Q^T from the linear fits, $\langle(Q^T - Q_{\text{fit}}^T)^2\rangle$, where the ensemble average is performed over all observations for which $\tau \geq \tau_c$. Figure 7 shows how $\langle(Q^T - Q_{\text{fit}}^T)^2\rangle$ decreases with increasing T, with a possible leveling off at $T \approx 300$ s. If observations around the Q_{fit}^T line were uncorrelated random events, then we would expect $\langle(Q^T - Q_{\text{fit}}^T)^2\rangle$ to decay according to the Central Limit Theorem, i.e., as T^{-1}. The slower $T^{-1/2}$ decay in Figure 7 thus indicates temporal correlation in the transport system, probably associated with the correlated turbulence structures driving transport.

4.3. Timescale Bias in Stress Determination

[26] Prediction of aeolian sediment flux depends on determining the amount of stress in excess of a specific threshold, τ_c. Disregarding, for now, problems inherent in determination of the stress threshold, we wish simply to highlight how the occurrence of intermittent transport around a threshold introduces a timescale bias in transport prediction. Figure 8a shows how the mean ($\langle\tau_{\log}^T\rangle$) and variance ($\text{Var}[\tau_{\log}^T]$) of shear stress distributions computed over the duration of the deployment decline systematically with T. Changes in the observed stress distributions, especially those that occur near the transport threshold, influence derivation of the stress-flux relationship.

[27] Figure 8b shows distributions of $\tau_{\log}^T$ for four averaging durations: 1, 10, 60, and 300 s. All of the distributions appear to be log normal, though there is a slight narrowing and rightward shift of the distributions for larger T, reflecting the decrease with T of $\text{Var}[\tau_{\log}^T]$ shown in Figure 8a. To our knowledge, little has been written about the distribution of aeolian surface shear stresses, though wind velocities (roughly the square root of shear stress) appear to follow right-skewed thin-tailed distributions [*Barchyn and Hugenholtz*, 2011] consistent with our observed log-normal stress distributions.

[28] Assuming a transport law with saltation flux growing linearly with excess stress as in equation (14), the mean excess shear stress, $\langle\tau_{\text{ex}}^T\rangle = \langle\tau_{\log}^T - \tau_c\rangle$, provides a direct predictor of transport with which Q should grow proportionately. For a time series of varying shear stresses, $\langle\tau_{\text{ex}}^T\rangle$ depends on the probability distribution of τ^T, i.e.,

$$\langle\tau_{\text{ex}}^T\rangle = \langle(\tau^T - \tau_c)\,|\tau^T > \tau_c\rangle P(\tau^T > \tau_c) = \int_{\tau_c}^{\infty} (\tau^T - \tau_c) f(\tau^T)\mathrm{d}\tau^T. \tag{15}$$

The above expression states that the overall mean excess stress depends on the mean excess stress during above-threshold periods multiplied by the probability that stress is above threshold, $P(\tau^T > \tau_c)$. $f(\tau^T)$ is the probability density of stresses for a specific T. Presuming, as observed, that $f(\tau^T)$ is log-normally distributed with timescale-dependent scale and shape parameters, σ^T and μ^T, respectively, determined from the mean and variance of the stress distributions found above as $\sigma^T = \sqrt{\ln\left(1 + \frac{\text{Var}[\tau^T]}{\langle\tau_{\log}^T\rangle^2}\right)}$ and $\mu^T = \ln(\langle\tau_{\log}^T\rangle) - \frac{1}{2}(\sigma^T)^2$, yields an explicit expression for estimating $\langle\tau_{\text{ex}}^T\rangle$ in equation (15):

$$\langle\tau_{\text{ex}}^T\rangle = \left(\frac{1}{2}\right)\left[\exp\left(\mu^T + \frac{(\sigma^T)^2}{2}\right)\left(1 + \text{erf}\left[\frac{\mu^T + (\sigma^T)^2 - \ln(\tau_c)}{\sqrt{2}\sigma^T}\right]\right)\right.$$
$$\left. -\tau_c\left(1 + \text{erf}\left[\frac{\mu^T - \ln(\tau_c)}{\sqrt{2}\sigma^T}\right]\right)\right], \tag{16}$$

where "erf" is the error function. Here for simplicity, we assume the constant $\tau_c = 0.060$ Pa ($U_{*,c} = 0.22$ m/s) used earlier for computation of U_*. Figure 8c shows both observed values of $\langle\tau_{\text{ex}}^T\rangle$ and computations by equation (16). The plot indicates that equation (16) provides a reasonable method of accounting for the scaling of excess stress

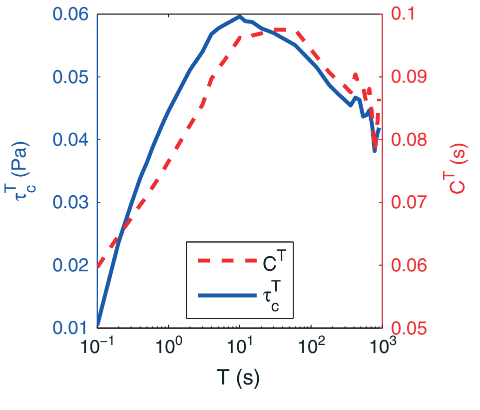

Figure 6. Estimates of τ_c^T and C^T by least-squares linear regression fit to equation (14) for a range of timescales, T.

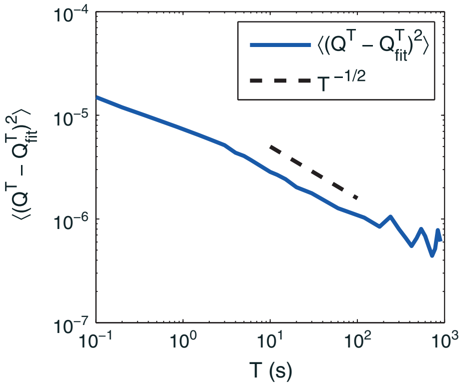

Figure 7. Evolution of observational scatter, $\langle (Q^T - Q^T_{\mathrm{fit}})^2 \rangle$, with increasing averaging timescale, T. The scatter decreases systematically with increasing T up to about 300 s, after which it appears to level out. $\langle (Q^T - Q^T_{\mathrm{fit}})^2 \rangle$ scales as $T^{-1/2}$ (solid black line), whereas the Central Limit Theorem, for uncorrelated observations, predicts scaling as T^{-1}. This discrepancy likely reflects temporal correlation in sediment transport interactions with atmospheric turbulence.

with T, and it supports the notion that intermittency contributes to timescale bias in calculation of τ_{ex}. However, we note that this prediction is directly determined by knowledge of how the parameters $\langle \tau^T_{\mathrm{log}} \rangle$ and $\mathrm{Var}[\tau^T_{\mathrm{log}}]$ vary with T. Broader applicability of equation (16) to determine the effect of timescale on mean excess shear stress depends on understanding the timescale dependence of $\langle \tau^T_{\mathrm{log}} \rangle$ and $\mathrm{Var}[\tau^T_{\mathrm{log}}]$, a point which is beyond the scope of this article.

4.4. Wind Variability

[29] The strong dependence of stress calculations on T can partially be explained by the scale-dependent nature of turbulent wind fluctuations. To understand the nature of atmospheric turbulence at our site, we computed autocorrelations and second-order structure functions [e.g., *Frisch*, 1995] of the Run 4 wind velocity time series. The streamwise and vertical wind velocity autocorrelations, ρ_{uu} and ρ_{ww}, respectively, were calculated based on the detrended time series, $u - \langle u \rangle$ and $w - \langle w \rangle$, where $\langle u \rangle$ and $\langle w \rangle$ were calculated as the means over the duration of Run 4. These autocorrelation curves, shown in Figure 9a, offer evidence for long-time correlation in u far exceeding that of w. The decay of ρ_{uu} indicates correlation up to a time lag of $\Delta t \approx 300$ s. Autocorrelation of vertical wind, ρ_{ww}, decays much more quickly (up to a time lag of $\Delta t \approx 1$ s), indicating relatively negligible temporal correlation.

[30] The u structure function, $\langle (\Delta u)^2 \rangle$, describes how mean-squared differences in instantaneous streamwise wind, u, grow with increasing time interval, Δt. The u structure function in Figure 9b indicates that streamwise wind fluctuations grow without bound through the duration of the time series. Up to $\Delta t \approx 3$ s, structure function growth scaling as $\sim (\Delta t)^{2/3}$ indicates inertial subrange behavior [*Frisch*, 1995]. Beyond 3 s, velocity fluctuations continue to grow, though at a slower pace with $\sim (\Delta t)^{1/5}$. In contrast to u, the w structure function, $\langle (\Delta w)^2 \rangle$, shows negligible growth of vertical velocity fluctuations for increasing Δt. The unrestrained growth of $\langle (\Delta u)^2 \rangle$ suggests that horizontal velocity fluctuations occur at a wide range of overlapping timescales ranging from turbulent structures to meteorological variability. The nonstationary nature of u fluctuations, in turn, may explain why the streamwise wind velocity autocorrelation, ρ_{uu}, takes much longer to decay than the vertical velocity autocorrelation, ρ_{ww}.

[31] That streamwise wind fluctuations display correlated behavior up to 300 s and experience variability that continues to grow beyond the duration of our measurements helps to explain the above observations of timescale dependence in calculation of shear stress. In particular, for determination of the Reynolds stress, estimates of u' by equation (4) will tend to grow for larger T because of the increasing variability of velocity fluctuations indicated by Figure 9b. In general, the observed nonstationarity of wind fluctuations appears to preclude the choice of a single optimal timescale for computation of shear stress.

4.5. Threshold Hysteresis and Lag Effects

[32] We have thus far considered how turbulent wind variability affects determination of the stress-flux relationship,

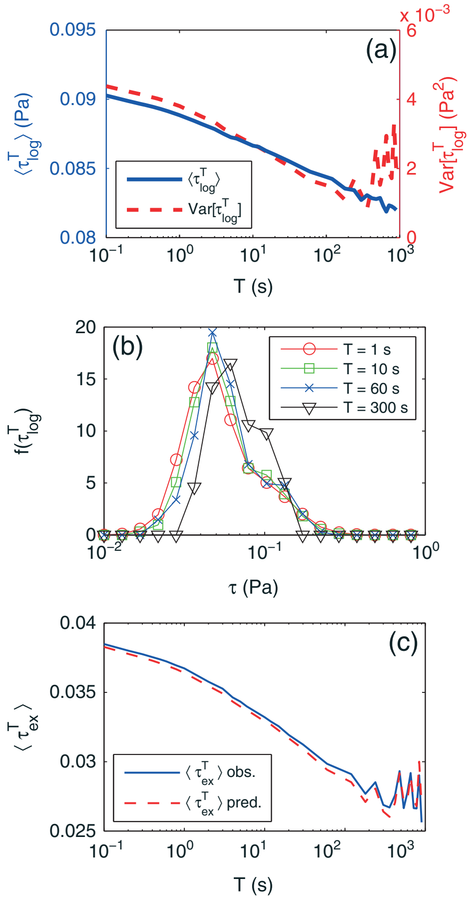

Figure 8. (a) Mean, $\langle \tau^T_{\mathrm{log}} \rangle$, and variance, $\mathrm{Var}[\tau^T_{\mathrm{log}}]$, of all stress estimates versus averaging timescale, T. (b) Probability density of stress distribution, $f(\tau^T_{\mathrm{log}})$, calculated at four averaging timescales, T. (c) Mean excess shear stress, $\langle \tau^T_{\mathrm{ex}} \rangle$, versus T. Assuming a log-normal shear stress distribution described by the timescale-dependent means and variances shown in Figure 8a, it is possible to predict the timescale dependence of $\langle \tau^T_{\mathrm{ex}} \rangle$.

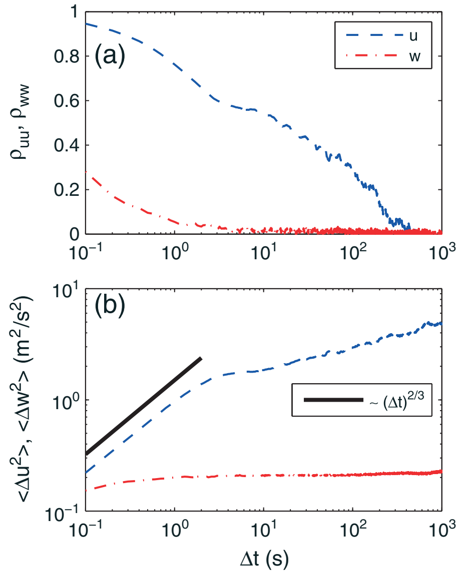

Figure 9. (a) Streamwise and vertical velocity autocorrelations, ρ_{uu} and ρ_{ww}, respectively, versus time lag, Δt, during Run 4. While ρ_{ww} decays quickly, the slow-decaying ρ_{uu} indicates that correlations in u persist up to $\Delta t \approx 300$ s. (b) Second-order structure functions of wind velocity fluctuations, computed as ensemble averages of squared velocity differences, $\langle \Delta u^2 \rangle$ and $\langle \Delta w^2 \rangle$, versus time interval, Δt, for streamwise velocity, u, and vertical velocity, w, respectively, during Run 4. The structure function for u shows $\sim \Delta t^{2/3}$ inertial subrange scaling up to 3 s, then it continues to grow more slowly after this time ($\sim \Delta t^{1/5}$). In contrast, the structure function for w displays negligible growth.

especially during intermittent transport. These considerations have implicitly assumed a single threshold value, τ_c, for initiation and cessation of saltation and an instantaneous response of transport to changes in shear stress. Now, we consider the presence of hysteresis effects introduced by different aerodynamic and collision threshold stresses, $\tau_{c,\mathrm{aero}}$ and $\tau_{c,\mathrm{col}}$, for initiation and cessation of motion, respectively, and transport lags associated with these processes.

[33] To quantify the role of lags and hysteresis in our system, we consider instances of initiation and cessation of saltation. For our system, we operationally define initiation (cessation) as transport (no transport) occurring after at least one full second of $Q = 0$ ($Q > 0$). Within our data series, we find 88 such initiation and 89 cessation events. For each initiation (cessation), we take $t_{\mathrm{init}} = 0$ ($t_{\mathrm{cess}} = 0$) as the first instance of transport (no transport), then we compute ensemble averages of Q, u, and w for a 20-second window around each t_{init} and t_{cess}. The resulting ensemble-averaged time series are shown in Figure 10.

[34] During transport initiation, wind velocity reaches a peak value of $U_{\mathrm{init}} \approx 8.7$ m/s, then declines toward a steady state ≈ 8.0 m/s for continued sustenance of transport. For cessation, wind velocity decreases gradually toward a minimum value of $U_{\mathrm{cess}} \approx 6.8$ m/s at the time when transport ceases. The difference between U_{init} and U_{cess} hints at a difference between $\tau_{c,\mathrm{aero}}$ and $\tau_{c,\mathrm{col}}$. We plug U_{init} into equation (1) (assuming a lack of saltation roughness at the onset of motion) to estimate an aerodynamic threshold shear velocity, $U_{*,c,\mathrm{aero}} = 0.27$ m/s. Similarly, we apply equation (6) (accounting for saltation roughness) to compute $U_{*,c,\mathrm{col}} = 0.21$ m/s from U_{cess}. Based on these values, we find that $U_{*,c,\mathrm{col}}/U_{*,c,\mathrm{aero}} = 0.76$, close to the 0.82 ratio observed by *Bagnold* [1937]. Based on the U_* thresholds, we find $\tau_{c,\mathrm{aero}} = 0.093$ Pa and $\tau_{c,\mathrm{col}} = 0.053$ Pa. These values span a wide range covering a large portion of the stress values observed during our field campaign (Figure 8b).

[35] In addition to the different aerodynamic and collision threshold values, Figure 10 also indicates significant lags in the threshold crossings. Prior to initiation, $\langle u \rangle$ steadily increases toward its peak value over a period of ≈ 5 s. Upon initiation, $\langle Q \rangle$ increases rapidly over ≈ 1 s toward its peak value, while $\langle u \rangle$ declines toward a steady state value of ≈ 8 m/s. $\langle Q \rangle$ also declines slightly after reaching its peak value, possibly indicating the "overshoot" and equilibration process produced by numerical models [*Anderson and Haff*,

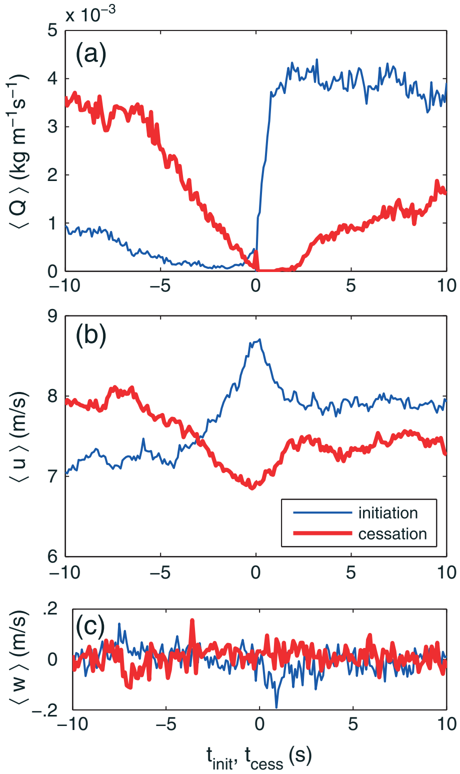

Figure 10. (a) Ensemble-averaged time series of sediment flux, $\langle Q \rangle$, around instances of sediment transport initiation and cessation. t_{init} and t_{cess} are relative times, with $t_{\mathrm{init}} = 0$ and $t_{\mathrm{cess}} = 0$ referring to times of first initiation and cessation of motion, respectively. (b) The ensemble-averaged streamwise wind, $\langle u \rangle$, suggests a higher "aerodynamic" threshold wind speed for initiation compared to the "collision" threshold for cessation, and comparison of $\langle u \rangle$ to $\langle Q \rangle$ indicates the presence of transport lags. (c) Ensemble-averaged vertical wind, $\langle w \rangle$, shows a slight downward dip for $t_{\mathrm{init}} \approx 1$ s, possibly reflecting the influence of turbulent sweeps on aerodynamic initiation of transport; otherwise, the effect of $\langle w \rangle$ on initiation and cessation of transport appears to be negligible.

1988, 1991; *McEwan and Willetts*, 1991; *Shao and Raupach*, 1992; *McEwan and Willetts*, 1993], but it could also simply reflect the simultaneous post-peak decline in $\langle u \rangle$. The cessation process occurs as a simultaneous gradual $\approx$ 5 s decline in $\langle Q \rangle$ and $\langle u \rangle$. $\langle w \rangle$ shows almost no correspondence to the initiation and cessation processes, providing a possible explanation for the poor performance of the Reynolds stress (which incorporates the fluctuating wind component) as a predictor of transport rates. There is a slight dip in $\langle w \rangle$ at $t_{\text{init}} \approx 1$ s, indicating the possible role of turbulent sweeps on initiating particle motion; however, the timing of this negative $\langle w \rangle$ excursion a full second after transport initiation indicates that it may simply be a random blip in the time series. We also note that, while lag effects are apparent in the initiation and cessation of transport, an analysis of cross correlations between u, w, and Q, indicated negligible lags between these time series, possibly due to spanwise separation of the instruments.

5. Discussion

[36] Our results suggest that saltation sand flux, Q, grows linearly with excess shear stress, $\tau_{\text{ex}} = \tau - \tau_c$, but specific parameterization of this relationship depends on averaging timescale, T, and choice of log law versus Reynolds stress method. In general, the log law derived stress, $\tau_{\log}$, provides better predictions of Q than the Reynolds stress, τ_{Re}, especially for smaller T. This may be explained by the fact that our estimates of $\tau_{\log}$, particularly at short timescales, are based on the streamwise wind, which, through its influence on the drag force experienced by saltating grains, may more directly determine Q than does τ [*Butterfield*, 1991; *Sterk et al.*, 1998; *Leenders et al.*, 2005]. In this sense, our results match closely with the work of *Jackson and McCloskey* [1997], who observed correspondence between simultaneous measurements of sand flux and the square of horizontal wind speed. Also, because the Reynolds stress is computed based on calculation of fluctuating wind speeds relative to average values, calculations of τ_{Re} are more sensitive to the nonstationarity of wind velocity statistics prevalent during our deployment at White Sands.

[37] We note that some scatter in the observed Q-τ relationship may be related to the $\approx$ 0.7 m spanwise separation between wind and sediment flux observations at our site, which was intended to reduce interference among instruments. *Baas and Sherman* [2005] observed strong transport heterogeneity over length scales of tens of centimeters associated with aeolian streamers. We therefore expect that wind velocities measured by the ultrasonic anemometer could have been somewhat different from those driving saltation into the Wenglor laser particle counters. Based on an observed mean transverse wind velocity magnitude of $|v| = 1.4$ m/s, we estimate a characteristic time of 0.5 s for transverse advection of turbulent structures between the anemometer and Wenglors.

[38] While instrument separation is a real issue, we note that transport does not simply respond to local wind conditions. Sediment transport sensors detect mobile particle trajectories initiated at a range of locations spanning a distance beginning several meters upwind of the sensor. Spatial variations in turbulence statistics and surface properties upwind of the sensor will therefore affect locally observed transport rates and thresholds [e.g., *Davidson-Arnott et al.*, 2005, 2008; *Barchyn and Hugenholtz*, 2011]. Further confirmation of differences between our estimated "collision" and "aerodynamic" transport thresholds described in section 4.5, therefore, requires understanding of how sediment transport structures are advected downwind and respond nonlocally to fluctuations in wind velocity. However, we note that observed transport initiation and cessation events may be equally affected by advection of upwind structures; thus, the presence of such structures may be canceled out in determination of the impact and aerodynamic thresholds. A full accounting for such spatial and temporal correlations (both streamwise and transverse) in wind and transport requires deployment of high-frequency multi-instrument arrays as by *Baas and Sherman* [2005].

[39] While wind direction remained uniform through the duration of our deployment, errors in our analysis may have also arisen due to consideration only of the streamwise component of horizontal wind. Our observations show that the mean wind angle (relative to prevailing) was $\langle |\tan^{-1}(v/u)| \rangle = 10.8°$ leading to a mean difference between total horizontal and prevailing wind of $\langle \sqrt{u^2 + v^2}/u \rangle = 1.03$, indicating that errors associated with consideration only of the streamwise wind component were relatively minor. Inclusion of the transverse wind measurements would have further complicated our analysis with questions of how to properly average the vector sum of wind components, but this issue should be addressed in the future. Also, while the Wenglors could respond to changes in wind direction by rotating on their stand, the response time of this rotation is uncertain.

[40] In choosing averaging timescales, a fundamental tension arises. On the one hand, longer averaging durations offer improved statistical convergence and complete accounting for turbulent fluctuations. However, longer averaging obscures short-term transport intermittency and variability. Rather than applying arbitrary averaging timescales, it would then be appealing to define physically relevant averaging times for field observations. For example, the integral timescale is commonly applied to describe the maximum duration of turbulent fluctuations. This is particularly important for Reynolds stress, whose estimation depends on an ensemble average of fluctuating wind components. *van Boxel et al.* [2004] argued that Reynolds stress computations must sample sufficiently long periods to capture the largest eddies, and that the sampling period increases with instrument height and decreases with wind speed. Estimating the turbulence integral timescale based on the time for full decorrelation of ρ_{uu} in Figure 9a yields an integral timescale of $T_{\text{int}} \approx 300$ s. This also happens to be the approximate time for convergence of the Q-τ relationship (Figure 7).

[41] Despite the suggestion of an integral timescale of $T_{\text{int}} = 300$ s, fit parameters of the Q-τ relationship continue to change beyond $T = 300$ s (Figure 6), as do values of the u structure function (Figure 9b). Similarly, *Guo et al.* [2012] found systematic changes in flux predictions for wind averaging times up to 1 h. These observations call into question whether it is really possible to choose a timescale for which wind velocity statistics are stationary. Even beyond the integral timescale, large-scale coherent structures, such as hairpin vortices, continue to generate correlations in u [e.g., *Guala et al.*, 2011], while synoptic wind variation, caused

by changes in meteorological forcing, induce nonstationarity in the wind record at even longer timescales [*Panofsky and Dutton*, 1984]. *Metzger et al.* [2007] chose a stationary timescale based on a power spectral gap between shorter turbulent and longer meteorological fluctuations. However, we calculated power spectra (not shown here) for our wind velocity time series and found no such spectral gap.

[42] While longer averaging times could potentially provide near-stationary turbulence statistics, they do not account for transport intermittency, lags, and threshold hysteresis. Our observations show in particular how intermittent transport introduces strong timescale effects in calculation of shear stress. For example, we have proposed a method for calculating shear velocity to account for changes in aerodynamic roughness height induced by the presence of a saltation layer. By assuming a constant focal height and velocity, it is theoretically possible to avoid dealing with systematic increase in roughness height with saltation intensity. However, our method still depends on distinguishing between periods with and without transport. We did this by assuming a single threshold shear stress; however, this led to timescale-dependent estimates of $\langle \tau_{\mathrm{ex}}^{T} \rangle$ due to transport intermittency. Ideally, then, saltation flux estimates should account for the true roughness adjustment time. *McEwan and Willetts* [1993] noted that adjustments in the velocity profile persist for up to 40 s and that the velocity profile deviates from a logarithmic form during transient adjustments. At shorter times, there are also lags for saltation flux to respond to near-surface winds [e.g., *Anderson and Haff*, 1988; *Butterfield*, 1998; *Spies et al.*, 2000]. In addition, presence of separate aerodynamic and collision thresholds introduces path dependence in prediction of overall sediment flux [*Rasmussen and Sorensen*, 1999; *Kok*, 2010], even without the complicating effect of local changes in τ_c related to surface sediment moisture and cohesiveness variations [e.g., *Gillette et al.*, 1996; *Davidson-Arnott and Bauer*, 2009].

[43] Pending specific physical knowledge of lagged adjustment timescales, threshold hysteresis, and spatial correlations, it may be possible to derive scaling relationships to account for scale effects, as has been done in models of fluvial landscape evolution [e.g., *Passalacqua et al.*, 2006]. Equation (16), for example, offers an example of how, based on knowledge of the timescale dependence of wind statistics, one could relate excess shear stress calculated from different time-averaging windows during intermittent transport. Such rescaling could perhaps depend on the "relative wind strength" parameter defined by *Stout and Zobeck* [1997], which describes the wind coefficient of variation relative to mean and threshold wind, and the "intermittency factor" described by *Rasmussen and Sorensen* [1999] for the relative frequency of transport. However, these and other [e.g., *Sorensen*, 1997] past attempts to account for intermittency effects have implicitly assumed stationary wind statistics during observation intervals (e.g., 5 min intervals used by *Stout and Zobeck* [1997]), an assumption that we observed to be violated. An additional problem with treatments of intermittency is that they depend strongly on instrument detection limits and arbitrarily chosen sampling times [e.g., *Barchyn and Hugenholtz*, 2011]. *Barchyn et al.* [2011] argue for some standardization of measurement techniques as a possible solution to this problem.

5.1. Prediction of Sediment Flux Based on Long-Term Meteorological Records

[44] *Bagnold* [1941] offered a method to predict long-term rates of dune migration based on the vector sum of wind speeds obtained from meteorological data. *Fryberger et al.* [1979] developed a similar method specifically adapted for utilization of World Meteorological Organization (WMO) standard wind records, which are determined hourly as 10 min averages of wind speed and direction recorded by anemometers 10 m above the ground [*WMO*, 2008]. Defining a "drift potential" to describe both the magnitude and directional variability of winds, Fryberger was able to relate Landsat observed dune morphologies to wind regimes at sites throughout the world. *Lancaster* [1985] applied similar methodology to explain dune morphologies in the Namib Sand Sea, and *Maia et al.* [2005] found that regional wind data predicted relative annual variations in dune migration rates. Based on WMO meteorological data obtained from a site several kilometers from the White Sands dune field, *Reitz et al.* [2010] and *Jerolmack et al.* [2012] predicted absolute rates of annual saltation flux that agreed closely with direct measurements of dune migration. Given the complex and intermittent response of saltation to high-frequency turbulent fluctuations, it is initially surprising that such low-resolution wind observations could reasonably predict aeolian transport rates.

[45] We consider our own observations in light of the success of sand flux predictions based on long-term meteorological records. We have found that the relationship between sediment flux and shear stress exhibits the greatest convergence for averaging timescales exceeding 300 s; other investigators [e.g., *Shao and Mikami*, 2005; *Davidson-Arnott et al.*, 2012] have also noted the increasing convergence of the stress-flux relationship at longer times. For comparison, in studies of fluvial bed load transport, it has been well documented that short-term observations are subject to broad stochastic variability [e.g., *Singh et al.*, 2009], and time-averaged predictions smooth out variability both in driving fluid turbulence and resulting transport rates [*Barry*, 2004; *Recking et al.*, 2012]. However, specific parameterizations of our empirical flux law (Figure 6) do not converge at any timescale. *Guo et al.* [2012], who evaluated Fryberger-like methods to determine daily sediment flux, found systematic variations in flux predictions for averaging times ranging from 1 to 60 min, especially when wind speeds were near the threshold of motion. It may be that an intermediate timescale, such as the WMO 10 min standard, may provide an ideal balance between short-term turbulent variability on the one hand and long-term meteorological variability on the other.

[46] In addition to timescale dependence of the flux law, we have also found that linear and 3/2 functional forms (i.e., the specific choice of n in equation (9)) for aeolian flux laws are almost indistinguishable near the threshold of motion (Figure 10). Given that most aeolian transport appears to occur near the threshold of motion [*Jerolmack and Brzinski*, 2010; *Jerolmack et al.*, 2011], choice of a specific flux law may therefore be relatively unimportant to long-term transport prediction. Choice of threshold stress is, in contrast, therefore extremely important for prediction, leading to particular problems at sites subject to a variety of threshold conditions [e.g., *Bauer et al.*, 2012].

Understanding how to account for the effect of changing roughness and different initiation/cessation thresholds is critical for future aeolian transport prediction.

[47] Whatever the appropriate timescale for prediction of aeolian sediment flux, more high-frequency observations are required for understanding the scale-dependence of sediment transport and wind observations. Such observations could constrain minimum observational timescales depending on spanwise instrument separation [e.g., *Baas and Sherman*, 2005] and instrument height [e.g., *van Boxel et al.*, 2004; *Leenders et al.*, 2005] while also providing information on lagged and hysteretic transport processes. Also, studies are needed to evaluate statistical limitations of short sampling windows [*Spies et al.*, 2000; *Namikas*, 2003]. At the very least, we hope that our analysis makes clear that timescale and measurement choices can substantially affect interpretations in field observation of aeolian saltation and that these effects must be explicitly addressed for proper comparison of field observations with equilibrium experimental, numerical, and analytical flux laws.

6. Conclusions

[48] We have performed a study to investigate the effects of time averaging on predictions of aeolian saltation flux. We have considered two methods for estimating shear stress—the logarithmic law-of-the-wall and Reynolds stress—and the time averaging implicit in both methods. We collected coupled high-frequency measurements of wind velocity and saltation flux during intermittent sand transport on a dune. Our data suggest a linear flux relationship of the form $Q = C(\tau - \tau_c)$, though a 3/2 transport law with $Q \sim (\tau - \tau_c)^{3/2}$ is equally plausible given that most transport occurs near the threshold of motion. Specific parameters of the flux relationship are strongly affected by choice of time-averaging interval, T, and do not converge. The correlation between Q and τ improves for increasing T, and log law estimates of τ more closely relate to Q than do Reynolds stress estimates.

[49] Estimates of shear stress are strongly affected by choice of T. To account for changes in aerodynamic roughness caused by momentum-extracting saltators, we adopted a modified log law, leading to a piecewise dependence of U_* on U. As a result of intermittency and frequent threshold crossings, estimates of excess stress, τ_{ex}^{T}, decline systematically with T. By noting that stress fluctuations are log-normally distributed and then determining how the mean and standard deviation of shear stress vary with T, we can reasonably account for the timescale bias in computation of excess stress. Streamwise wind velocity correlation persists up to ≈ 300 s, but the wind velocity structure function appears nonstationary even beyond this time, providing a potential explanation for the systematic variation in excess shear stress.

[50] In addition to the effects of time averaging during nonstationary winds and intermittent transport, our data indicate lags and hysteresis during the initiation and cessation of motion. We estimated an aerodynamic threshold shear stress, $\tau_{c,\mathrm{aero}} = 0.093$ Pa, for initiation of transport, which is almost double the collision threshold, $\tau_{c,\mathrm{col}} = 0.053$ Pa, for ceasing transport. In accord with past numerical models, we also found that initiation and cessation of motion do not occur instantaneously but as lagged processes with timescales on the order of seconds. Because wind stresses are mostly in this threshold range and flux laws are highly sensitive to choice of a threshold value, effects of threshold hysteresis and lags must be addressed in future high-frequency studies of aeolian saltation.

[51] Though time averaging appears to affect parameterization of saltation flux laws in natural environments at all timescales, improvement in correlation between Q and τ for increasing T suggests that predictions based on time-averaged values could offer improved confidence at least in relative predictions of aeolian saltation flux. Nonetheless, high-frequency observations are still necessary to improve understanding of aeolian saltation during unsteady turbulent winds and intermittent sediment transport.

[52] **Acknowledgments.** White Sands travel costs were partially supported by the Department of Earth and Environmental Science, University of Pennsylvania. R.L.M. acknowledges educational support from the U.S. National Science Foundation Graduate Research Fellowship. T.E.B. and C.H.H. acknowledge funding from the National Science and Engineering Council of Canada and Alberta Innovates. We thank Jasper Kok, Robin Davidson-Arnott, and an anonymous reviewer for their thoughtful and thorough commentary on the original manuscript. We also thank David Bustos and the National Park Service for facilitating our ongoing educational and research work at White Sands National Monument.

References

Almeida, M. P., J. S. Andrade, and H. J. Herrmann (2006), Aeolian transport layer, *Phys. Rev. Lett.*, *96*(1), 018001, doi:10.1103/PhysRevLett.96.018001.

Anderson, R. S., and P. K. Haff (1988), Simulation of eolian saltation, *Science*, *241*(4867), 820–823, doi:10.1126/science.241.4867.820.

Anderson, R. S., and P. K. Haff (1991), Wind modification and bed response during saltation of sand in air, *Acta Mech. (Suppl.)*, *1*, 21–51.

Anderson, R. S., and B. Hallet (1986), Sediment transport by wind: Toward a general model, *Geol. Soc. Am. Bull.*, *97*, 523–535.

Arens, S. M., H. M. E. Van Kaam-Peters, and J. H. Van Boxel (1995), Air flow over foredunes and implications for sand transport, *Earth Surf. Processes Landforms*, *20*(4), 315–332, doi:10.1002/esp.3290200403.

Baas, A. C. W. (2006), Wavelet power spectra of aeolian sand transport by boundary layer turbulence, *Geophys. Res. Lett.*, *33*, L05403, doi:10.1029/2005GL025547.

Baas, A. C. W., and D. J. Sherman (2005), Formation and behavior of aeolian streamers, *J. Geophys. Res.*, *110*, F03011, doi:10.1029/2004JF000270.

Bagnold, R. A. (1937), The transport of sand by wind, *Geog. J.*, *89*(5), 409–438, doi:10.2307/1786411.

Bagnold, R. A. (1938), The measurement of sand storms, *Proc. R. Soc. London, Ser. A*, *167*(929), 282–291.

Bagnold, R. A. (1941), *The Physics of Blown Sand and Desert Dunes*, Dover, London.

Barchyn, T. E., and C. H. Hugenholtz (2011), Comparison of four methods to calculate aeolian sediment transport threshold from field data: Implications for transport prediction and discussion of method evolution, *Geomorphology*, *129*(3-4), 190–203, doi:10.1016/j.geomorph.2011.01.022.

Barchyn, T. E., C. H. Hugenholtz, and J. T. Ellis (2011), A call for standardization of aeolian process measurements: Moving beyond relative case studies, *Earth Surf. Processes Landforms*, *36*(5), 702–705, doi:10.1002/esp.2136.

Barry, J. J. (2004), A general power equation for predicting bed load transport rates in gravel bed rivers, *Water Resour. Res.*, *40*, W10401, doi:10.1029/2004WR003190.

Bauer, B. O., J. Yi, S. L. Namikas, and D. J. Sherman (1998), Event detection and conditional averaging in unsteady aeolian systems, *J. Arid. Environ.*, *39*(3), 345–375, doi:10.1006/jare.1998.0380.

Bauer, B. O., C. A. Houser, and W. G. Nickling (2004), Analysis of velocity profile measurements from wind-tunnel experiments with saltation, *Geomorphology*, *59*(14), 81–98, doi:10.1016/j.geomorph.2003.09.008.

Bauer, B. O., R. G. D. Davidson-Arnott, I. J. Walker, P. A. Hesp, and J. Ollerhead (2012), Wind direction and complex sediment transport response across a beach-dune system, *Earth Surf. Processes Landforms*, *37*(15), 1661–1677, doi:10.1002/esp.3306.

Butterfield, G. R. (1991), Grain transport rates in steady and unsteady turbulent airflows, *Acta Mech. (Suppl.)*, *1*, 97–122.

Butterfield, G. R. (1998), Transitional behaviour of saltation: Wind tunnel observations of unsteady winds, *J. Arid. Environ.*, *39*(3), 377–394, doi:10.1006/jare.1997.0367.

Chapman, C., I. J. Walker, P. A. Hesp, B. O. Bauer, R. G. D. Davidson-Arnott, and J. Ollerhead (2013), Reynolds stress and sand transport over a vegetated foredune, *Earth Surf. Processes Landforms*, doi:10.1002/esp.3428, in press.

Chapman, C. A., I. J. Walker, P. A. Hesp, B. O. Bauer, and R. G. Davidson-Arnott (2012), Turbulent Reynolds stress and quadrant event activity in wind flow over a coastal foredune, *Geomorphology*, *151-152*, 1–12, doi:10.1016/j.geomorph.2011.11.015.

Creyssels, M., P. Dupont, A. O. El Moctar, A. Valance, I. Cantat, J. T. Jenkins, J. M. Pasini, and K. R. Rasmussen (2009), Saltating particles in a turbulent boundary layer: Experiment and theory, *J. Fluid Mech.*, *625*, 47–74, doi:10.1017/S0022112008005491.

Davidson-Arnott, R., and B. Bauer (2009), Aeolian sediment transport on a beach: Thresholds, intermittency, and high frequency variability, *Geomorphology*, *105*(1-2), 117–126, doi:10.1016/j.geomorph.2008.02.018.

Davidson-Arnott, R. G., K. MacQuarrie, and T. Aagaard (2005), The effect of wind gusts, moisture content and fetch length on sand transport on a beach, *Geomorphology*, *68*(1-2), 115–129, doi:10.1016/j.geomorph.2004.04.008.

Davidson-Arnott, R. G. D., Y. Yang, J. Ollerhead, P. A. Hesp, and I. J. Walker (2008), The effects of surface moisture on aeolian sediment transport threshold and mass flux on a beach, *Earth Surf. Processes Landforms*, *33*(1), 5574, doi:10.1002/esp.1527.

Davidson-Arnott, R. G. D., B. O. Bauer, I. J. Walker, P. A. Hesp, J. Ollerhead, and C. Chapman (2012), High-frequency sediment transport responses on a vegetated foredune, *Earth Surf. Processes Landforms*, *37*(11), 1227–1241, doi:10.1002/esp.3275.

Dong, Z., P. Lv, Z. Zhang, G. Qian, and W. Luo (2012), Aeolian transport in the field: A comparison of the effects of different surface treatments, *J. Geophys. Res.*, *117*, D09210, doi:10.1029/2012JD017538.

Duran, O., P. Claudin, and B. Andreotti (2011), On aeolian transport: Grain-scale interactions, dynamical mechanisms and scaling laws, *Aeolian Res.*, *3*(3), 243–270, doi:10.1016/j.aeolia.2011.07.006.

Ellis, J. T., B. Li, E. J. Farrell, and D. J. Sherman (2009), Protocols for characterizing aeolian mass-flux profiles, *Aeolian Res.*, *1*(1-2), 19–26, doi:10.1016/j.aeolia.2009.02.001.

Fan, L. T., and L. A. Disrud (1977), Transient wind erosion—Study of nonstationary effect on rate of wind erosion, *Soil Sci.*, *124*(1), 61–65, doi:10.1097/00010694-197707000-00011.

Farrell, E. J., D. J. Sherman, J. T. Ellis, and B. Li (2012), Vertical distribution of grain size for wind blown sand, *Aeolian Res.*, *7*, 51–61, doi:10.1016/j.aeolia.2012.03.003.

Frank, A., and G. Kocurek (1994), Effects of atmospheric conditions on wind profiles and aeolian sand transport with an example from White Sands National Monument, *Earth Surf. Processes Landforms*, *19*(8), 735–745, doi:10.1002/esp.3290190806.

Frisch, U. (1995), *Turbulence*, Cambridge University Press, Cambridge.

Fryberger, S. G., G. Dean, and E. D. McKee (1979), Dune forms and wind regime, in *A Study of Global Sand Seas, U.S. Geological Survey Professional Paper, 1052*, pp. 137–170.

Fryrear, D. W. (1986), A field dust sampler, *J. Soil Water Conserv.*, *41*(2), 117–120.

Gillette, D. A., G. Herbert, P. H. Stockton, and P. R. Owen (1996), Causes of the fetch effect in wind erosion, *Earth Surf. Processes Landforms*, *21*(7), 641–659.

Greeley, R., D. G. Blumberg, and S. H. Williams (1996), Field measurements of the flux and speed of wind-blown sand, *Sedimentology*, *43*(1), 41–52, doi:10.1111/j.1365-3091.1996.tb01458.x.

Guala, M., M. Metzger, and B. J. McKeon (2011), Interactions within the turbulent boundary layer at high Reynolds number, *J. Fluid Mech.*, *666*, 573–604, doi:10.1017/S0022112010004544.

Guo, Z., T. M. Zobeck, J. E. Stout, and K. Zhang (2012), The effect of wind averaging time on wind erosivity estimation, *Earth Surf. Processes Landforms*, *37*(7), 797–802, doi:10.1002/esp.3222.

Ho, T. D., A. Valance, P. Dupont, and A. Ould El Moctar (2011), Scaling laws in aeolian sand transport, *Phys. Rev. Lett.*, *106*(9), 094501, doi:10.1103/PhysRevLett.106.094501.

Hogstrom, U., J. C. R. Hunt, and A. S. Smedman (2002), Theory and measurements for turbulence spectra and variances in the atmospheric neutral surface layer, *Boundary Layer Meteorol.*, *103*, 101–124.

Hugenholtz, C. H., and T. E. Barchyn (2011), Laboratory and field performance of a laser particle counter for measuring aeolian sand transport, *J. Geophys. Res.*, *116*, F01010, doi:10.1029/2010JF001822.

Jackson, D. W. T., and J. McCloskey (1997), Preliminary results from a field investigation of aeolian sand transport using high resolution wind and transport measurements, *Geophys. Res. Lett.*, *24*(2), 163–166, doi:10.1029/96GL03967.

Jackson, P. S., and J. C. R. Hunt (1975), Turbulent wind flow over a low hill, *Q. J. R. Meteorolog. Soc.*, *101*(430), 929–955, doi:10.1002/qj.49710143015.

Jerolmack, D. J., and T. A. Brzinski (2010), Equivalence of abrupt grain-size transitions in alluvial rivers and eolian sand seas: A hypothesis, *Geology*, *38*(8), 719–722, doi:10.1130/G30922.1.

Jerolmack, D. J., D. Mohrig, J. P. Grotzinger, D. A. Fike, and W. A. Watters (2006), Spatial grain size sorting in eolian ripples and estimation of wind conditions on planetary surfaces: Application to Meridiani Planum, Mars, *J. Geophys. Res.*, *111*, E12S02, doi:10.1029/2005JE002544.

Jerolmack, D. J., M. D. Reitz, and R. L. Martin (2011), Sorting out abrasion in a gypsum dune field, *J. Geophys. Res.*, *116*, F02003, doi:10.1029/2010JF001821.

Jerolmack, D. J., R. C. Ewing, F. Falcini, R. L. Martin, C. Masteller, C. Phillips, M. D. Reitz, and I. Buynevich (2012), Internal boundary layer model for the evolution of desert dune fields, *Nat. Geosci.*, *5*(3), 206–209, doi:10.1038/ngeo1381.

Kaimal, J. C., and J. J. Finnigan (1994), *Atmospheric Boundary Layer Flows: Their Structure and Measurement*, Oxford University Press, Oxford.

Kawamura, R. (1951), Study of sand movement by wind, *Rep. Inst. Sci. Technol.*, *5*, 95–112.

Klose, M., and Y. Shao (2012), Stochastic parameterization of dust emission and application to convective atmospheric conditions, *Atmos. Chem. Phys.*, *12*, 7309–7320, doi:10.5194/acp-12-7309-2012.

Klose, M., and Y. Shao (2013), Large-eddy simulation of turbulent dust emission, *Aeolian Res.*, *8*, 49–58, doi:10.1016/j.aeolia.2012.10.010.

Kok, J. F. (2010), Difference in the wind speeds required for initiation versus continuation of sand transport on Mars: Implications for dunes and dust storms, *Phys. Rev. Lett.*, *104*(7), 074502, doi:10.1103/PhysRevLett.104.074502.

Kok, J. F. (2011), A scaling theory for the size distribution of emitted dust aerosols suggests climate models underestimate the size of the global dust cycle, *PNAS*, *108*(3), 1016–1021, doi:10.1073/pnas.1014798108.

Kok, J. F., and N. O. Renno (2008), Electrostatics in wind-blown sand, *Phys. Rev. Lett.*, *100*(1), 014501, doi:10.1103/PhysRevLett.100.014501.

Kok, J. F., E. J. R. Parteli, T. I. Michaels, and D. B. Karam (2012), The physics of wind-blown sand and dust, *Rep. Prog. Phys.*, *75*(10), 106901, doi:10.1088/0034-4885/75/10/106901.

Lancaster, N. (1985), Winds and sand movements in the Namib Sand Sea, *Earth Surf. Processes Landforms*, *10*(6), 607–619, doi:10.1002/esp.3290100608.

Langford, R. P. (2003), The Holocene history of the White Sands dune field and influences on eolian deflation and playa lakes, *Quat. Int.*, *104*(1), 31–39, doi:10.1016/S1040-6182(02)00133-7.

Leenders, J. K., J. H. van Boxel, and G. Sterk (2005), Wind forces and related saltation transport, *Geomorphology*, *71*(3-4), 357–372, doi:10.1016/j.geomorph.2005.04.008.

Lettau, H., and K. Lettau (1977), Experimental and micrometeorological field studies of dune migration, in *Exploring the World's Driest Climate (IES Report, 101)*, pp. 110–147, University of Wisconsin-Madison, Institute for Environmental Studies, Madison, WI.

Li, B., and C. McKenna Neuman (2012), Boundary-layer turbulence characteristics during aeolian saltation, *Geophys. Res. Lett.*, *39*, L11402, doi:10.1029/2012GL052234.

Li, B., D. J. Sherman, E. J. Farrell, and J. T. Ellis (2010), Variability of the apparent von Karman parameter during aeolian saltation, *Geophys. Res. Lett.*, *37*, L15404, doi:10.1029/2010GL044068.

Lu, H., and Y. Shao (1999), A new model for dust emission by saltation bombardment, *J. Geophys. Res.*, *104*(D14), 16827–16842, doi:10.1029/1999JD900169.

Maia, L. P., G. S. S. Freire, and L. D. Lacerda (2005), Accelerated dune migration and aeolian transport during El Nino events along the NE Brazilian coast, *J. Coast. Res.*, *216*, 1121–1126, doi:10.2112/03-702A.1.

McEwan, I. K., and B. B. Willetts (1991), Numerical model of the saltation cloud, *Acta Mech. (Suppl.)*, *1*, 53–66.

McEwan, I. K., and B. B. Willetts (1993), Adaptation of the near-surface wind to the development of sand transport, *J. Fluid Mech.*, *252*, 99–115, doi:10.1017/S0022112093003684.

McKenna Neuman, C., and W. G. Nickling (1994), Momentum extraction with saltation: Implications for experimental evaluation of wind profile parameters, *Boundary Layer Meteorol.*, *68*(1-2), 35–50, doi:10.1007/BF00712663.

Metzger, M., B. J. McKeon, and H. Holmes (2007), The near-neutral atmospheric surface layer: Turbulence and non-stationarity, *Philos. Trans. R. Soc. A*, *365*(1852), 859–876, doi:10.1098/rsta.2006.1946.

Namikas, S. L. (2003), Field measurement and numerical modelling of aeolian mass flux distributions on a sandy beach, *Sedimentology*, *50*(2), 303–326, doi:10.1046/j.1365-3091.2003.00556.x.

Namikas, S. L., and D. J. Sherman (1997), Predicting aeolian sand transport: Revisiting the White model, *Earth Surf. Processes Landforms*, *22*(6), 601–604.

Namikas, S. L., B. O. Bauer, and D. J. Sherman (2003), Influence of averaging interval on shear velocity estimates for aeolian transport modeling, *Geomorphology*, *53*(3-4), 235–246, doi:10.1016/S0169-555X(02)00314-8.

Owen, P. R. (1964), Saltation of uniform grains in air, *J. Fluid Mech.*, *20*(02), 225–242, doi:10.1017/S0022112064001173.

Pahtz, T., J. F. Kok, and H. J. Herrmann (2012), The apparent roughness of a sand surface blown by wind from an analytical model of saltation, *New J. Phys.*, *14*(4), 043035, doi:10.1088/1367-2630/14/4/043035.

Panofsky, H. A., and J. A. Dutton (1984), *Atmospheric Turbulence: Models and Methods for Engineering Applications*, Wiley, New York.

Passalacqua, P., F. Porte-Agel, E. Foufoula-Georgiou, and C. Paola (2006), Application of dynamic subgrid-scale concepts from large-eddy simulation to modeling landscape evolution, *Water Resour. Res.*, *42*, W06D11, doi:10.1029/2006WR004879.

Rasmussen, K. R., and H. E. Mikkelsen (1998), On the efficiency of vertical array aeolian field traps, *Sedimentology*, *45*(4), 789–800, doi:10.1046/j.1365-3091.1998.00179.x.

Rasmussen, K. R., and M. Sorensen (1999), Aeolian mass transport near the saltation threshold, *Earth Surf. Processes Landforms*, *24*(5), 413–422.

Rasmussen, K. R., and M. Sorensen (2008), Vertical variation of particle speed and flux density in aeolian saltation: Measurement and modeling, *J. Geophys. Res.*, *113*, F02S12, doi:10.1029/2007JF000774.

Recking, A., F. Libault, C. Peteuil, and T. Jolimet (2012), Testing bedload transport equations with consideration of time scales, *Earth Surf. Processes Landforms*, *37*(7), 774–789, doi:10.1002/esp.3213.

Reitz, M. D., D. J. Jerolmack, R. C. Ewing, and R. L. Martin (2010), Barchan-parabolic dune pattern transition from vegetation stability threshold, *Geophys. Res. Lett.*, *37*, L19402, doi:10.1029/2010GL044957.

Schonfeldt, H.-J., and S. von Lowis (2003), Turbulence-driven saltation in the atmospheric surface layer, *Meteorol. Z.*, *12*(5), 257–268, doi:10.1127/0941-2948/2003/0012-0257.

Shao, Y., and M. Mikami (2005), Heterogeneous saltation: Theory, observation and comparison, *Boundary Layer Meteorol.*, *115*(3), 359–379, doi:10.1007/s10546-004-7089-2.

Shao, Y., and M. R. Raupach (1992), The overshoot and equilibration of saltation, *J. Geophys. Res.*, *97*(D18), 20559–20564, doi:10.1029/92JD02011.

Sherman, D. J. (1992), An equilibrium relationship for shear velocity and apparent roughness length in aeolian saltation, *Geomorphology*, *5*(3-5), 419–431, doi:10.1016/0169-555X(92)90016-H.

Sherman, D. J., and E. J. Farrell (2008), Aerodynamic roughness lengths over movable beds: Comparison of wind tunnel and field data, *J. Geophys. Res.*, *113*, F02S08, doi:10.1029/2007JF000784.

Sherman, D. J., and B. Li (2012), Predicting aeolian sand transport rates: A reevaluation of models, *Aeolian Res.*, *3*(4), 371–378, doi:10.1016/j.aeolia.2011.06.002.

Sherman, D. J., D. W. Jackson, S. L. Namikas, and J. Wang (1998), Wind-blown sand on beaches: An evaluation of models, *Geomorphology*, *22*(2), 113–133, doi:10.1016/S0169-555X(97)00062-7.

Singh, A., K. Fienberg, D. J. Jerolmack, J. Marr, and E. Foufoula-Georgiou (2009), Experimental evidence for statistical scaling and intermittency in sediment transport rates, *J. Geophys. Res.*, *114*, F01025, doi:10.1029/2007JF000963.

Sorensen, M. (1997), On the effect of time variability of the wind on rates of aeolian sand transport, *Aarhus Geosci.*, *7*, 73–77.

Sorensen, M. (2004), On the rate of aeolian sand transport, *Geomorphology*, *59*(1-4), 53–62, doi:10.1016/j.geomorph.2003.09.005.

Spies, P.-J., I. K. McEwan, and G. R. Butterfield (2000), One-dimensional transitional behaviour in saltation, *Earth Surf. Processes Landforms*, *25*(5), 505–518.

Sterk, G., A. F. G. Jacobs, and J. H. Van Boxel (1998), The effect of turbulent flow structures on saltation sand transport in the atmospheric boundary layer, *Earth Surf. Processes Landforms*, *23*(10), 877–887.

Stout, J. E., and T. M. Zobeck (1997), Intermittent saltation, *Sedimentology*, *44*(5), 959–970, doi:10.1046/j.1365-3091.1997.d01-55.x.

Ungar, J. E., and P. K. Haff (1987), Steady state saltation in air, *Sedimentology*, *34*(2), 289–299, doi:10.1111/j.1365-3091.1987.tb00778.x.

van Boxel, J. H., G. Sterk, and S. M. Arens (2004), Sonic anemometers in aeolian sediment transport research, *Geomorphology*, *59*(1-4), 131–147, doi:10.1016/j.geomorph.2003.09.011.

von Karman, T. (1930), *Mechanische Ahnlichkeit und Turbulenz*, Weidmannsche Buchh., Berlin.

Walker, I. J. (2005), Physical and logistical considerations of using ultrasonic anemometers in aeolian sediment transport research, *Geomorphology*, *68*(1-2), 57–76, doi:10.1016/j.geomorph.2004.09.031.

Werner, B. T. (1990), A steady-state model of wind blown sand transport, *J. Geol.*, *98*, 1–17.

White, B. R. (1982), Two-phase measurements of saltating turbulent boundary layer flow, *Int. J. Multiphase Flow*, *8*(5), 459–473, doi:10.1016/0301-9322(82)90018-0.

Williams, G. (1964), Some aspects of the eolian saltation load, *Sedimentology*, *3*(4), 257–287, doi:10.1111/j.1365-3091.1964.tb00642.x.

WMO (2008), *Guide to Meteorological Instruments and Methods of Observation,* 7th ed., World Meteorological Organization No. 8, World Meteorological Organization, Geneva.